

Low-Fe(III) Greenalite Was a Primary Mineral from Neoproterozoic Oceans

Jena E Johnson^{*a}, Janet R Muhling^{b,c}, Julie Cosmidis^{a,1}, Birger Rasmussen^c, Alexis S Templeton^a

^aDept. of Geosciences, University of Colorado - Boulder, 2200 Colorado Ave, Boulder CO 80309

^bSchool of Earth Sciences, The University of Western Australia, 35 Stirling Highway, Crawley WA 6009, Australia

^cDept. of Applied Geology, Curtin University, Kent Street, Bentley, Perth WA 6102, Australia

¹Currently Dept. of Geosciences, Pennsylvania State University, University Park, PA 16802

*Corresponding Author: jenaje@umich.edu; Currently Dept. of Earth and Environmental Sciences, University of Michigan, Ann Arbor, MI 48109

Key Points

- Neoproterozoic nanoparticle silicate inclusions appear to be the earliest iron mineral preserved in cherts from Australia and South Africa
- Our multiscale analyses indicate the particles are greenalite that are dominantly Fe(II) but also have low and variable Fe(III) content
- We present four (bio)geochemical hypotheses that could produce low-Fe(III) greenalite

This is the author manuscript accepted for publication and has undergone full peer review but has not been through the copyediting, typesetting, pagination and proofreading process, which may lead to differences between this version and the Version of Record. Please cite this article as doi: [10.1002/2017GL076311](https://doi.org/10.1002/2017GL076311)

Abstract

1 Banded iron formations (BIFs) represent chemical precipitation from Earth's early oceans and
2 therefore contain insights into ancient marine biogeochemistry. However, BIFs have undergone
3 multiple episodes of alteration, making it difficult to assess the primary mineral assemblage.
4 Nanoscale mineral inclusions from 2.5 billion-year-old BIFs and ferruginous cherts provide new
5 evidence that iron silicates were primary minerals deposited from the Neoproterozoic ocean,
6 contrasting sharply with current models for BIF formation. Here we used multi-scale imaging
7 and spectroscopic techniques to characterize the best-preserved examples of these inclusions.
8 Our integrated results demonstrate that these early minerals were low-Fe(III) greenalite. We
9 present potential pathways in which low-Fe(III) greenalite could have formed through changes in
10 saturation state and/or iron oxidation and reduction. Future constraints for ancient ocean
11 chemistry and early life's activities should include low-Fe(III) greenalite as a primary mineral in
12 the Neoproterozoic ocean.

Index Terms:

0404 Anoxic and hypoxic environments
0414/4912 Biogeochemical cycles, processes, and modeling
0471 Oxidation/reduction reactions
1042/ 3620 Mineral and crystal chemistry
9623 Archean

Keywords: *banded iron formations, iron silicates, Precambrian, nanoparticle inclusions, chert*

13 **Introduction**

14 For the first half of Earth's ~4.5 billion-year history, there was negligible atmospheric oxygen
15 and the oceans had high levels of ferrous iron and silica. The sedimentary record from 3.8 to 2.3
16 billion years ago (Ga) documents the survival of oxygen-sensitive detrital grains in
17 conglomerates and marine sandstones (Johnson et al. 2014, Rasmussen & Buick 1999), the lack
18 of terrestrial iron oxidation in paleosols (Prasad & Roscoe 1996, Rye & Holland 1998), and an
19 unfamiliar sulfur cycle with strong signals of photochemical reactions occurring in the absence
20 of an ozone layer (Farquhar et al. 2011). Another conspicuous difference from modern marine
21 sediments was the deposition of extensive silica-rich Banded Iron Formations (BIFs) in the early
22 oceans. These laminated BIFs are thought to be comprised of chemical precipitates accumulating
23 in ferruginous and silica-rich oceans (Bekker et al. 2014, Beukes & Gutzmer 2008). BIFs have
24 been extensively investigated as one of the best records of marine chemistry in the Archean [4.0
25 - 2.5 Ga] oceans (e.g. Klein 2005). However, it is also well-established that these BIFs have
26 experienced early and late diagenesis, fluid flow, and metamorphism over their multi-billion-
27 year existence, and therefore many—if not all—minerals in BIFs are attributed to diagenesis and
28 later alteration (e.g., Bekker et al. 2014, Beukes 1984, Fischer & Knoll 2009, Klein 2005, Pufahl
29 & Hiatt 2012, Simonson 2003). Identifying the original precipitate(s) of BIFs has therefore been
30 a critical question pertinent to understanding what BIFs represent and record with respect to
31 ancient seawater chemistry and early life. While it is impossible to pinpoint the amorphous
32 precursor phases that originally formed in the water column, it is possible to determine the first
33 stable crystalline minerals that formed under Archean ocean conditions and were preservable in
34 the rock record – which we will call the “primary mineral(s).”

35

36 While initial suggestions of primary BIF minerals concentrated on iron silicates like glauconite
37 or greenalite (Leith 1903, Spurr 1894, Winchell et al. 1899), later models converged on iron
38 oxides such as hematite (Cloud 1973, James 1954, reviewed in Rasmussen et al. 2017).
39 Observations of chert bands and nodules, often targeted because they were early-forming and
40 relatively impermeable to later altering fluids (e.g., Clout & Simonson 2005), resulted in the
41 discoveries of microcrystalline ($< 1 \mu\text{m}$) hematite particles that supported the conclusion that
42 hematite was paragenetically the primary iron mineral (Ayres 1972, Beukes & Gutzmer 2008,
43 Klein & Beukes 1989, Spencer & Percival 1952, Sun et al. 2015). This hematite was proposed to
44 derive from the dehydration of ferric oxyhydroxide precipitates settling from suspension into
45 silica gel on the ocean floor, with earlier hematite particles then getting replaced by coarser
46 crystals of magnetite and siderite during diagenesis (Beukes & Gutzmer 2008). This conclusion
47 also made sense from a solubility point of view: oxidizing iron from soluble iron (ferrous
48 $\text{Fe}^{2+}_{(\text{aq})}$) to insoluble iron oxides (e.g., $\text{Fe}(\text{III})(\text{OH})_3_{(\text{s})}$) would act as a mechanism to transport
49 iron into the sediments to form precursor BIFs. Previous research has extensively explored the
50 processes that could produce these putative ferric oxyhydroxides in Archean oceans (e.g., see
51 review by Posth et al. 2014), while other studies have used the adsorption behavior of trace
52 metals and nutrients onto iron oxides to produce geologic records of seawater chemistry (e.g.,
53 Bjerrum & Canfield 2002, Frei et al. 2009, Konhauser et al. 2009).
54
55 However, recent re-examinations of Neoproterozoic BIF-hosted chert from the ~2.5 Ga Hamersley
56 Group in Western Australia and ~2.5 Ga Transvaal Supergroup in South Africa using nanoscale
57 imaging and elemental analyses have led to the suggestion that iron silicate phases were actually
58 present earlier than hematite (Rasmussen et al. 2015, 2016, 2017). Drill core samples of well-

59 preserved BIFs and iron-rich cherts contained nanometer-sized iron silicate particles, as well as
60 often bearing several morphologies of hematite and other iron minerals. Hematite either
61 mineralized as a replacement texture such as iron oxide rims on iron silicate and iron-bearing
62 carbonate crystals, or occurred as individual 100 nm – 10 μ m equant or platy particles and
63 defined primary bedding but transitioned vertically and horizontally to submicron iron silicate
64 particles (Rasmussen et al. 2016). These iron silicates were identified as stilpnomelane and/or
65 greenalite and occurred as randomly oriented plates that vary in size from <10 nm to 1 μ m
66 (Rasmussen et al. 2015, 2016, 2017). These observations were all highly suggestive of hematite
67 being a secondary mineral, formed after primary iron silicates (Rasmussen et al. 2016), which
68 was further explored and supported by recent experimental studies (Tosca et al. 2016).

69
70 If iron silicates are indeed the earliest mineral that we can identify in BIFs, then we need to
71 better characterize them to understand what they record about the ancient marine system. Our
72 goals were twofold: 1) to determine the exact mineralogy of the best-preserved examples of these
73 iron silicate inclusions, which serves to constrain Archean seawater chemistry; and 2) to assess
74 the redox state of iron in these iron silicates, which can be indicative of the paleo-ocean
75 oxidation state and potentially reveal any microbial involvement in the precipitation of these
76 phases. We used a variety of bulk, microscale, and nanoscale techniques to characterize the iron
77 silicate mineralogy and the iron redox state present in particles from the well-preserved examples
78 of ancient BIF-hosted cherts. We find the best-preserved iron silicate nano-inclusions are
79 greenalite with low and variable levels of Fe^{3+} , and these new results enable us to discuss several
80 possible hypotheses to explain the deposition of primary low-Fe(III) greenalite that led to the
81 formation of the most recognizable early Earth sediment, Banded Iron Formations.

82

83 **Materials and Methods**

84 Nanoparticle-bearing samples were acquired from ~2.5 Ga BIF and ferruginous chert hosted in
85 well-preserved cores from Western Australia and South Africa (see Rasmussen et al. 2015, 2017;
86 Sumner & Bowring 1996 for core locations). These cores included ABDP9, GKF, DDH44, and
87 Silvergrass, which have all undergone only low-grade metamorphism and are considered sub-
88 greenschist facies (Miyano & Beukes 1984, Smith et al. 1982). Ferruginous cherts from ABDP9
89 and GKF were prioritized because they possessed the most finely laminated sections with the
90 best level of detail of the many examined samples and were less recrystallized than BIF-hosted
91 chert. Two samples were also chosen to ensure that our findings represented BIF mineralogy as
92 well as ferruginous chert: DDH44 388.3 m was chosen as one of the best-preserved Hamersley
93 BIFs; and Silvergrass 313.6 m was included as another example of a BIF with some well-
94 preserved chert bands, although other bands showed recrystallization and late crystals of
95 riebeckite and magnetite.

96

97 Samples were prepared as bulk powders, thin sections, and ~100 nm thick foils to examine the
98 nanoparticles using a variety of chemical and structural characterization techniques. See
99 Supporting Information for preparation and analytical details. Focused Ion Beam (FIB)-prepared
100 foils for nanoscale analyses were produced from samples ABDP9 219.3 m and 288.2 m, GKF
101 327.2 m, and from the Silvergrass core at 313.6 m. The iron redox state of the FIB foils was
102 examined at the nanoscale using synchrotron transmission X-ray microscopy (STXM) at the iron
103 L edge on beamline 10ID-1 (SM) at the Canadian Light Source in Saskatoon, Canada (Cosmidis
104 & Benzerara 2014). Using this technique, we assessed the iron redox state across a single particle

105 and compared the redox state variation between neighboring particles within any foil, following
106 the Fe-silicate method and calibration established by Bourdelle et al (2013). These nanoscale
107 redox data were paired with subsequent Transmission Electron Microscopy (TEM)-based
108 examinations to confirm the particle-scale mineralogy and assess the recrystallization extent of
109 individual particles. Bright-field TEM and high-angle annular dark-field scanning TEM images
110 were collected to examine particle textures, and qualitative and quantitative Energy Dispersive
111 Spectroscopy (EDS) maps, spectra, and point analyses were collected to help identify the
112 nanoparticle mineralogy. Because the particles can be damaged by the electron beam, especially
113 during electron diffraction, we analyzed high-resolution TEM images using a fast fourier
114 transform algorithm to produce diffractograms in which lattice spacing could be quantitatively
115 measured and compared to iron silicate standards.

116

117 **Results**

118 We primarily used transmission-based microscopic and spectroscopic techniques to assess the
119 morphology and crystal structure of the iron-rich inclusions, complemented by microscale and
120 bulk spectroscopic and diffraction techniques. The iron silicate inclusions from five well-
121 preserved samples derived from Australia and South Africa displayed differential
122 recrystallization, with some samples (e.g., ABDP9 288.3 m) containing fairly pristine particles
123 and other samples (e.g., ABDP9 219.3 m and GKF 327.2 m) having some highly recrystallized
124 inclusions associated with chert cavities. Diffractograms yielded d-spacings corresponding to a 7
125 Ångstrom clay in most sections (Figure 1). This result was consistent with analyses that showed
126 small 7 Ångstrom clay peaks in bulk powders containing nanoparticle inclusions (Figure S1). Fe
127 X-ray absorption spectra plotted using Sixpack (Webb 2005) were also consistent with iron in a

128 silicate mineral (SI, Fig S2, S3). Using TEM-EDS, we confirmed that these particles only
129 contained Fe, Si, and O, with low and varying amounts of Mg and Al (Fig S4A-D, Table S1),
130 indicating these were Fe-silicates such as the 7 Ångstrom layered Fe-silicates greenalite
131 $[\text{Fe}^{2+}_3\text{Si}_2\text{O}_5(\text{OH})_4]$ or cronstedtite $[(\text{Fe}^{2+}, \text{Fe}^{3+})_3(\text{Si}, \text{Fe}^{3+})_2\text{O}_5(\text{OH})_4]$. The 7 Ångstrom silicates also
132 contained the ~20 Ångstrom structural modulation characteristic of greenalite (Fig 1)
133 (Guggenheim et al. 1982). The integrated results from all of our multi-scale independent
134 analyses indicate that the structure and chemistry of the nanoparticles were consistent with
135 greenalite.

136
137 Several other iron minerals were additionally observed. ABDP9 288 m2 contained siderite
138 euhedra and ABDP9 219 m had two small pyrite crystals, but both appeared secondary to the
139 greenalite as they were blocky crystals that cross-cut greenalite nanoparticles. In contrast to the
140 other sections, some silicate particles from section Silvergrass 313.6 m had 10 Ångstrom spacing
141 (Figure 1). These diffraction results coincided with a different elemental pattern (Figure S4E).
142 The data from this distinct set of particles were consistent with the presence of a 10 Ångstrom
143 layered silicate containing K, Fe, Mg, and Al cations, like the complex hydrated phyllosilicate
144 stilpnomelane $[(\text{K}, \text{Ca}, \text{Na})(\text{Fe}, \text{Mg}, \text{Al})_8(\text{Si}, \text{Al})_{12}(\text{O}, \text{OH})_{36} \cdot n\text{H}_2\text{O}]$ (Figure 1, Figure S4E). While
145 commonly found in low-pressure, sub-greenschist facies BIF, stilpnomelane is often considered
146 a metamorphic mineral associated with greenschist facies or glaucophane-schist facies
147 (Krivovichev 2013). In BIFs, stilpnomelane is generally observed texturally as forming
148 secondarily, associated with recrystallization and metamorphism (Feininger 1984, Klein 1974),
149 and this Silvergrass sample in thin section appeared petrographically to be more recrystallized
150 and altered. Therefore, we suggest that the stilpnomelane particles in Silvergrass 313.6 m are

151 alteration products from earlier greenalite inclusions. Another possibility is that the
152 stilpnomelane reflects detrital grains from volcanic sources (Haugaard et al. 2016, Laberge 1986,
153 Pickard 2002). Because all ten samples that we examined contained well-preserved greenalite
154 encased in chert, our results indicate greenalite was a primary mineral forming from Neoproterozoic
155 seawater.

156
157 The iron redox state of the iron silicate inclusions in these FIB foil samples were determined
158 using scanning transmission X-ray spectromicroscopy at the Fe L_{2,3} edge. We harnessed a novel
159 iron redox mapping method to examine the variability of the iron redox state at a nanoscale.
160 Following the protocol outlined in Bourdelle et al (2013), Fe(III)/Fe_{Total} maps were produced
161 across the iron-bearing nanoparticles (Figure 2) using the aXis2000 software (Hitchcock 2014).
162 This mapping indicated that the iron silicate inclusions were principally Fe(II), consistent with
163 Fe K-edge analyses (Fig S5), but the nanoparticles also contained low levels of Fe(III). Across
164 individual nanoparticles mapped for Fe(III) content, pixels ranged from 0% to >70%
165 Fe(III)/Fe_{Total} (Figure 2). The most pristinely preserved particles, those fully encased in chert,
166 had low ferric iron contents ranging from ~10% to 20% Fe(III)/Fe_{Total} (Figure 2). The low levels
167 of Fe(III) varied both within individual particles and between particles, and appeared unrelated to
168 the pixel position in the particle, particle orientation or particle location.

169
170 **Discussion**

171 One of our best windows into the chemistry and biology of early Earth's oceans is through
172 understanding what chemical precipitates were forming directly from seawater. While iron
173 oxyhydroxides were thought to be the dominant Fe minerals that initially precipitated, and were

174 therefore intensively studied for how they may reflect biological activities and elemental cycles
175 (Bekker et al. 2014, Kappler & Newman 2004, Konhauser et al. 2007, Posth et al. 2014), recent
176 observations of nanoscale iron silicate inclusions in early diagenetic, low-porosity chert have
177 called the existing model into question (Rasmussen et al. 2015, 2017). These iron silicates are
178 interpreted to be paragenetically earlier than iron oxides (Rasmussen et al. 2016), stimulating
179 new questions about what BIFs actually indicate about seawater chemistry and mineralization
180 pathways.

181
182 Additional factors make these pervasive iron silicate inclusions a compelling initial mineral
183 during BIF deposition. Iron silicates such as minnesotaite, greenalite, and stilpnomelane have
184 long been identified in BIFs, but the consensus view categorized these as secondary minerals or
185 derived from volcanic input (Beukes & Gutzmer 2008, Fischer & Knoll 2009, Haugaard et al.
186 2016, Klein 2005). There had been speculation that primary iron silicates could form in deeper-
187 water and more alkaline environments as ferrous iron and silica reacted, but these minerals were
188 not thought to be the major primary iron phase in BIFs (e.g., Beukes & Gutzmer 2008, Klein
189 1974). However, primary magnetic remanence that should have been recorded in original
190 hematite precipitates, if they stayed below 600 °C, have never been found in the Australian
191 Hamersley Group and South African Transvaal Supergroup BIFs (Abrajevitch et al. 2014, de
192 Kock et al. 2009, Humbert et al. 2017, Li et al. 1993) – highly suggestive of hematite being
193 emplaced secondarily. Additionally, with the probable elevated silica levels of the Archean
194 ocean (Maliva et al. 2005, Siever 1992, Stefurak et al. 2014), the mineralization of iron silicates
195 is thermodynamically predicted (Bethke 2002) from highly reducing oceans with $<10^{-56}$ atm of
196 O₂ (Fig S7).

197

198 To better constrain these potentially primary Neoproterozoic minerals, we fully characterized the
199 mineralogy and iron redox state of the best-preserved iron silicate inclusions that have been
200 discovered thus far. Ten samples from ~2.5 Ga BIFs and ferruginous cherts from diverse
201 localities in Australia and South Africa contain a single identical iron silicate mineral: greenalite.
202 From these observations, we argue that greenalite is the earliest iron mineral preserved in these
203 cherts. Earlier hypotheses had suggested that iron was deposited in the sediments as a result of
204 iron oxidation. In order to determine whether an oxidation state change was still relevant to
205 understanding deposition of primary iron silicates, we examined whether Fe(III) was present in
206 the greenalite particles and quantified how much ferric iron was present at the scale of individual
207 particles. In the most unaltered particles, we found that greenalite was dominantly Fe(II) with 10-
208 20% Fe(III). Fe(III) content was variable within individual particles and between particles. The
209 possibility that these low levels of Fe(III) were secondarily acquired cannot be ruled out;
210 however, the absence of a spatially-coherent redox distribution suggests that this Fe(III) was an
211 original component of the greenalite rather than oxidized by a secondary fluid front.

212

213 Our characterization of the Fe-rich nanoparticle inclusions enables us to consider and build on
214 existing hypotheses to explore the genesis of low-Fe(III) greenalite preserved in early chert. In
215 the following scenarios, our working hypothesis is that seawater silica (H_4SiO_4) was at saturation
216 with amorphous silica ($10^{-2.71}$ M, Rimstidt & Barnes 1980). Previous work has established that
217 silica levels were significantly higher in the Archean oceans (Maliva et al. 2005, Siever 1992)
218 and observations of primary authigenic silica granules in Archean cherts (Stefurak et al. 2014,
219 2015) provide strong evidence for silica levels at saturation with amorphous silica. We thus

220 assume amorphous silica was being deposited on the sea floor, encasing greenalite inclusions
221 during the diagenetic transformation into chert nodules and bands. In the models described
222 below, we primarily focus on various iron cycle hypotheses to result in the preservation of low-
223 Fe(III) greenalite in chert.

224

225 1. A straightforward explanation for the deposition of greenalite nanoparticles is that the
226 ferrous iron and silica concentrations of the ocean exceeded greenalite saturation (Figure
227 3-1). The saturation of greenalite is set by its solubility constant, which can be calculated
228 to lie at $10^{14.01}$ using estimates from Eugster and Chou (Eugster & Chou 1973). If we
229 assume dissolved silica was fixed at $10^{-2.71}$ M and pH at this time was ~ 7 (Halevy &
230 Bachan 2017), then greenalite would saturate when ferrous iron reached 30 nM (Fig S7).
231 This estimate is likely far lower than the concentrations that metastable precursor phases
232 would require to precipitate; however, it is useful to consider the thermodynamic
233 predictions for greenalite precipitation. Alternatively, ferrous iron could remain below 30
234 nM and increases in pH could trigger the precipitation of greenalite. These iron
235 concentrations are strikingly low and emphasize the ease with which greenalite should
236 precipitate from the Neoproterozoic ocean – and suggest that greenalite precipitation would
237 act as a limit to ferrous iron levels and pH.

238

239 The idea that greenalite was thermodynamically stable in the Neoproterozoic ocean expands
240 on early suggestions for iron silicate precipitation in deep waters (Beukes & Gutzmer
241 2008), which was also re-proposed when iron silicates were discovered as abundant
242 inclusions in chert (Rasmussen et al. 2015). A similar abiotic model has recently been

243 explored experimentally by Tosca et al (2016), who synthesized a proto-greenalite gel
244 under plausible Archean seawater conditions with high silica and iron concentrations at
245 pHs ≥ 7.5 . These experiments demonstrated that it is remarkably simple and favorable to
246 precipitate a precursor silicate gel in anoxic, ferruginous, and silica-rich oceans (Tosca et
247 al. 2016), and they suggested that alkaline hydrothermal waters upwelling into more
248 acidic CO₂-buffered surface water would rapidly nucleate greenalite. Rasmussen et al
249 (2017) expanded on this pH-focused model but proposed flipping the environmental
250 conditions: iron and silica delivered by more acidic vent fluids could then mix with more
251 alkaline seawater, initiating the precipitation of greenalite.

252

253 2. Greenalite solubility is still not well constrained and little is currently known about
254 whether the presence of Fe(III) would enhance the precipitation of greenalite. However, it
255 is hypothesized that in the iron-phosphate system, the oxidation of Fe(II) causes the
256 precipitation of Fe(II,III)-phosphate minerals (Cosmidis et al. 2014, Miot et al. 2009,
257 Voegelin et al. 2013). Furthermore, earlier work has shown that iron silicates, including
258 Fe(III) serpentine-member clays, can precipitate in silica-rich systems both abiotically
259 and stimulated by bacterial surfaces (Konhauser & Ferris 1996, Konhauser & Urrutia
260 1999, Urrutia & Beveridge 1994). If Fe(III) does change the thermodynamic properties of
261 greenalite and makes precipitation more favorable, then it is possible that waters
262 undersaturated with respect to Fe(II)-greenalite could have precipitated Fe(III)-bearing
263 greenalite upon aqueous Fe²⁺ oxidation (Figure 3-2). A variety of iron oxidation
264 mechanisms are known, including abiotic UV-radiation catalysis, microbial iron-
265 oxidizing photosynthesis, and biologically-mediated or abiotic interactions between

266 ferrous iron and oxygen (e.g., see Konhauser et al, 2007). Oxidation of iron in
267 ferruginous and silica-rich water could catalyze the precipitation of a low-Fe(III)
268 greenalite phase that could then be preserved in amorphous silica gel, eventually
269 mineralizing as greenalite inclusions in chert (Figure 3-2A).

270
271 Alternatively, iron oxidation in silica-rich water could initially produce high-Fe(III)
272 greenalite. However, in a ferruginous ocean, contact between Fe(III)-bearing clays and
273 fluids with ferrous iron could reduce structural Fe(III) and increase the Fe(II) content of
274 the mineral (Schaefer et al. 2011). Although we see no evidence for surface-associated
275 Fe(III) phases, these should be produced if adsorbed Fe(II) was oxidized; however, if
276 formed, such phases would be highly reactive in a reducing environment. A net chemical
277 reduction of Fe(III)-bearing greenalite could occur both during descent of the particles
278 through a ferruginous water column or in porewaters if reductants are present (Figure 3-
279 2B). The potential reactions described above could have led to a similar primary mineral
280 assemblage as model 1 and 2A – initial BIFs dominated by low-Fe(III) greenalite and
281 chert (Figure 3-2). Additionally, Fe(III) in the silicate structure or Fe(III) phases
282 associated with greenalite could have been reduced by bacterial respiration during early
283 diagenesis, resulting in an isostructural transformation to lower-Fe(III) clays or reductive
284 dissolution of the Fe-silicates into its constituent cations (Figure 3-2B) (Dong et al.
285 2009).

286
287 3. A third model would also form low-Fe(III) greenalite as a stable mineral product, but
288 from an initial Fe(II,III) precursor metastable phase: green rust

289 $[\text{Fe(II)}_4\text{Fe(III)}_2(\text{OH})_{12}^{2+} \cdot \text{CO}_3^{2-} \cdot 2\text{H}_2\text{O}$ or $\text{Fe(II)}_3\text{Fe(III)}(\text{OH})_8^+ \cdot \text{Cl} \cdot n\text{H}_2\text{O}]$ (Figure 3-3), as
290 suggested in a recent paper (Halevy et al. 2017). If a small proportion of aqueous iron is
291 oxidized –by any biological or abiotic mechanism discussed above– in a highly
292 ferruginous aqueous environment, then green rust is the metastable initial product that
293 forms in both laboratory experiments and environmental settings (Halevy et al. 2017,
294 Zegeye et al. 2012). Because green rust is a metastable phase, it would transform to
295 secondary, stable phases (Halevy et al. 2017). Ferrous iron present in both the ocean and
296 porewaters, as well as adsorbed and dissolved silica, could have subsequently induced the
297 transformation of green rust into thermodynamically more favorable low-Fe(III)
298 greenalite during particle descent and early diagenesis in the sediments (Figure 3-3).
299 Early diagenesis could also include iron-reducing microbes utilizing the oxidized iron in
300 green rust and promoting the transformation of green rust into the more stable Fe(II)-rich
301 greenalite. If the porewater conditions were supersaturated with respect to greenalite and
302 the oxidation potential (Eh) of the system was low enough, then the predicted stable iron
303 mineral to be preserved in the BIF sediments would be greenalite (Fig S7A).

304
305 4. Alternatively, it is possible that the oxidation of aqueous Fe(II) initially formed
306 metastable Fe(III) oxides with adsorbed silica, similar to prior suggestions (Fischer &
307 Knoll 2009), that then stabilized as greenalite in the water column or sediments (Figure
308 3-4). Indeed, experiments with modern iron-oxidizing phototrophs grown with 2 mM
309 silica resulted in the formation of Fe(III)-oxyhydroxides, with some changes to
310 morphology and crystallinity, silica substitution into the iron oxides, and co-precipitation
311 of amorphous silica (Eickhoff et al. 2014, Gauger et al. 2016, Wu et al. 2014). It is

312 notable that the formation of Fe(III) clays was not observed in these experiments, even
313 with high silica levels. However, it is still an open question as to whether iron oxides and
314 adsorbed silica would undergo dissolution and reprecipitation into low-Fe(III) greenalite
315 under reducing conditions and/or through the activities of Fe-reducing microbes (Fischer
316 & Knoll 2009), as this has not conclusively been shown to occur (Posth et al. 2013, but
317 see Aller et al. 1986).

318
319 It is currently difficult to resolve which model is most plausible to generate the low-Fe(III)
320 greenalite that we observe. The first abiotic saturation hypothesis is appealing in its simplicity,
321 and the low and variable levels of Fe(III) that we measured in the greenalite could be present as a
322 result of the equilibrium environmental conditions at the time of formation or, alternatively,
323 structural Fe(II) oxidation (Gorski et al. 2012) from secondary fluids post-lithification.
324 Alternatively, the low Fe(III) that we measure in the greenalite could signify original iron
325 oxidation from UV radiation, iron-oxidizing photosynthesis, or interactions with low levels of
326 oxygen. Another line of evidence for original Fe(III) present in greenalite or precursor phases
327 may arise from the Fe-rich carbonates present in BIFs, which many have argued are products of
328 early diagenesis, primarily based on the ^{12}C -enriched carbon isotopes and textures of these
329 phases (Ayres 1972, Becker & Clayton 1972, Beukes et al. 1990, Dimroth & Chauvel 1973,
330 Fischer & Knoll 2009, Johnson et al. 2013, Klein 1974, Walker 1984). Intriguingly, siderite is
331 also found as a product from the reduction of Fe(III)-bearing clays (Dong et al. 2009, Komlos et
332 al. 2007, Kostka et al. 1999). Therefore, hypotheses that involve a flux of oxidized iron –in Fe-
333 silicates or other phases– reaching the sediments and potentially undergoing microbial reduction
334 would be consistent with the arguments for early diagenetic Fe-rich carbonates in BIFs.

335
336
337
338
339
340
341
342
343
344
345
346
347
348

Distinguishing between hypotheses involving abiotic precipitation or iron oxidation followed by the stable mineralization of low-Fe(III) greenalite requires either further constraints on the solution chemistry and redox conditions of the 2.5 Ga ocean or more experimental data to measure what minerals actually precipitate in potential scenarios. Yet our detailed characterization of the earliest iron phases in BIF sediments as low-Fe(III) greenalite emplaces a firm target against which to compare experimental and environmental observations. For the primary mineral in equilibrium with the Neoproterozoic seawater to stabilize as greenalite rather than hematite, the deep ocean and/or porewater can be inferred to have an oxygen fugacity $<10^{-56}$ atm (Figure S7C) – inconsistent with the presence of extensive oxygenic photosynthesis. Going forward, to successfully recreate the chemistry and biology in the 2.5 Ga ocean, low-Fe(III) greenalite should be present in the stable mineral assemblage. Conversely, the presence of low-Fe(III) greenalite as a primary stable mineral 2.5 billion years ago should act as a constraint for future estimates of pH, ferrous iron, and silica concentrations in the Neoproterozoic ocean.

349
350

Acknowledgements

351
352
353
354
355
356
357
358
359
360
361
362
363
364
365
366

Supplemental data and results can be found in the Supporting Information and data used to generate figures can be found on the Deep Blue online repository [doi: 10.7302/Z2XS5SMK]. We appreciate the contributions of Eric Ellison on Fe XANES acquisition and analysis and Tyler Kane for performing bulk XRD measurements and assisting with XRD analyses using JADE software. We additionally are grateful to S. Guggenheim for providing a greenalite standard and to George Rossman for contributing a standard for cronstedtite and for his mineralogical consultations, as well as the helpful feedback from Nicholas Tosca and an anonymous reviewer. Samuel Webb and Ryan Davis greatly helped with our data acquisition from SSRL and Jian Wang provided calibration and assistance for our STXM measurements at CLS. We additionally thank Franck Bourdelle who kindly helped us produce the $\text{Fe}^{3+}/\text{Fe}_{\text{TOTAL}}$ maps. We acknowledge the Department of Mines and Petroleum, Western Australia, for access to drill-hole ABDP9 and the Council for Geoscience (South Africa) for access to drill-hole GKF. FIB and TEM analyses were performed at the Centre for Microscopy, Characterisation and Analysis, the University of Western Australia, a node of the Australian Microscopy and Microanalysis Research Facility funded from university and government sources. This research was funded by the Agouron

367 Institute (Postdoctoral Fellowship to J.E.J.) and the Rock-Powered Life NASA Astrobiology
368 Institute (Cooperative Agreement NNA15BB02A).

369 Portions of the research described in this paper was performed at the Canadian Light
370 Source, which is supported by the Canada Foundation for Innovation, Natural Sciences and
371 Engineering Research Council of Canada, the University of Saskatchewan, the Government of
372 Saskatchewan, Western Economic Diversification Canada, the National Research Council
373 Canada, and the Canadian Institutes of Health Research. Portions of this research were carried
374 out at the Stanford Synchrotron Radiation Lightsource, SLAC National Accelerator Laboratory,
375 which is supported by the U.S. Department of Energy, Office of Science, Office of Basic Energy
376 Sciences under Contract DE-AC02-76SF00515. The SSRL Structural Molecular Biology
377 Program is supported by the DOE Office of Biological and Environmental Research, and by the
378 National Institutes of Health, National Institute of General Medical Sciences (including
379 P41GM103393). The contents of this publication are solely the responsibility of the authors and
380 do not necessarily represent the official views of NIGMS or NIH.

381
382

383 **References**

- 384 Abrajevitch A, Pillans BJ, Roberts AP. 2014. Haematite pigmentation events and
385 palaeomagnetic recording: implications from the Pilbara Print Stone, Western Australia.
386 *Geophys. J. Int.* 199:658–72
- 387 Aller RC, Mackin JE, Cox Jr RT. 1986. Diagenesis of Fe and S in Amazon inner shelf muds:
388 apparent dominance of Fe reduction and implications for the genesis of ironstones. *Cont.*
389 *Shelf Res.* 6(1–2):263–89
- 390 Ayres DE. 1972. Genesis of Iron-bearing Minerals in Banded Iron Formation Mesobands in The
391 Dales Gorge Member, Hamersley Group, Western Australia. *Econ. Geol.* 67(8):1214–33
- 392 Becker RH, Clayton RN. 1972. Carbon isotopic evidence for the origin of a banded iron-
393 formation in Western Australia. *Geochim. Cosmochim. Acta.* 36(5):577–95
- 394 Bekker A, Planavsky NJ, Krapež B, Rasmussen B, Hofmann A, et al. 2014. Iron Formations:
395 Their Origins and Implications for Ancient Seawater Chemistry. *Treatise Geochem.*
396 *Second Ed.* 9:561–628
- 397 Bethke CM. 2002. *The Geochemist's Workbench: A User's Guide to Rxn, Act2, Tact, React, and*
398 *Gtplot, 4.0 Edition.* Urbana, IL: University of Illinois
- 399 Beukes NJ. 1984. Sedimentology of the Kuruman and Griquatown Iron-formations, Transvaal
400 Supergroup, Griqualand West, South Africa. *Precambrian Res.* 24(1):47–84
- 401 Beukes NJ, Gutzmer J. 2008. Origin and Paleoenvironmental Significance of Major Iron
402 Formations at the Archean-Paleoproterozoic Boundary. In *Banded Iron Formation-*
403 *Related High-Grade Ore*, Vol. 15, eds. S Hagemann, C Rosiere, J Gutzmer, N Beukes,
404 pp. 5–47
- 405 Beukes NJ, Klein C, Kaufman AJ, Hayes JM. 1990. Carbonate petrography, kerogen
406 distribution, and carbon and oxygen isotope variations in an early Proterozoic transition
407 from limestone to iron-formation deposition, Transvaal Supergroup, South Africa. *Econ.*
408 *Geol. Bull. Soc. Econ. Geol.* 85(4):663–90
- 409 Bjerrum CJ, Canfield DE. 2002. Ocean productivity before about 1.9 Gyr ago limited by
410 phosphorus adsorption onto iron oxides. *Nature.* 417(6885):159–62

- 411 Bourdelle F, Benzerara K, Beyssac O, Cosmidis J, Neuville DR, et al. 2013. Quantification of
412 the ferric/ferrous iron ratio in silicates by scanning transmission X-ray microscopy at the
413 Fe L_{2,3} edges. *Contrib. Mineral. Petrol.* 166(2):423–34
- 414 Cloud P. 1973. Paleocological Significance of the Banded Iron-Formation. *Econ. Geol.*
415 68(7):1135–43
- 416 Clout JMF, Simonson BM. 2005. Precambrian iron formations and iron formation-hosted iron
417 ore deposits. *Econ. Geol.* 100th Anniversary Volume:643–79
- 418 Cosmidis J, Benzerara K. 2014. Soft x-ray scanning transmission spectromicroscopy. In
419 *Biom mineralization Sourcebook: Characterization of Biominerals and Biomimetic*
420 *Materials*, eds. E DiMasi, LB Gower, pp. 115–33. CRC Press
- 421 Cosmidis J, Benzerara K, Morin G, Busigny V, Lebeau O, et al. 2014. Biomineralization of iron-
422 phosphates in the water column of Lake Pavin (Massif Central, France). *Geochim.*
423 *Cosmochim. Acta.* 126:78–96
- 424 de Kock MO, Evans DAD, Kirschvink JL, Beukes NJ, Rose E, Hilburn I. 2009. Paleomagnetism
425 of a Neoproterozoic-Paleoproterozoic carbonate ramp and carbonate platform succession
426 (Transvaal Supergroup) from surface outcrop and drill core, Griqualand West region,
427 South Africa. *Precambrian Res.* 169(1–4):80–99
- 428 Dimroth E, Chauvel J-J. 1973. Petrography of the Sokoman Iron Formation in Part of the Central
429 Labrador Trough, Quebec, Canada. *GSA Bull.* 84(1):111–34
- 430 Dong H, Jaisi DP, Kim J, Zhang G. 2009. Microbe-clay mineral interactions. *Am. Mineral.*
431 94(11–12):1505–19
- 432 Eickhoff M, Obst M, Schröder C, Hitchcock AP, Tylliszczak T, et al. 2014. Nickel partitioning in
433 biogenic and abiogenic ferrihydrite: The influence of silica and implications for ancient
434 environments. *Geochim. Cosmochim. Acta.* 140(Supplement C):65–79
- 435 Eugster HP, Chou I-M. 1973. The Depositional Environments of Precambrian Banded Iron-
436 Formations. *Econ. Geol.* 68(7):1144–68
- 437 Farquhar J, Zerkle AL, Bekker A. 2011. Geological constraints on the origin of oxygenic
438 photosynthesis. *Photosynth. Res.* 107(1):11–36
- 439 Feininger T. 1984. Stilpnomelane in metasomatic rocks associated with steatite and in regional
440 schists, Quebec Appalachians. *Can. Mineral.* 22(3):423–35
- 441 Fischer WW, Knoll AH. 2009. An Iron Shuttle for Deepwater Silica in Late Archean and Early
442 Paleoproterozoic Iron Formation. *Geol. Soc. Am. Bull.* 121(1–2):222–35
- 443 Frei R, Gaucher C, Poulton SW, Canfield DE. 2009. Fluctuations in Precambrian atmospheric
444 oxygenation recorded by chromium isotopes. *Nature.* 461(7261):250–53
- 445 Gauger T, Byrne JM, Konhauser KO, Obst M, Crowe S, Kappler A. 2016. Influence of organics
446 and silica on Fe(II) oxidation rates and cell–mineral aggregate formation by the green-
447 sulfur Fe(II)-oxidizing bacterium *Chlorobium ferrooxidans* KoFox – Implications for
448 Fe(II) oxidation in ancient oceans. *Earth Planet. Sci. Lett.* 443(Supplement C):81–89
- 449 Gorski CA, Aeschbacher M, Soltermann D, Voegelin A, Baeyens B, et al. 2012. Redox
450 Properties of Structural Fe in Clay Minerals. 1. Electrochemical Quantification of
451 Electron-Donating and -Accepting Capacities of Smectites. *Environ. Sci. Technol.*
452 46(17):9360–68
- 453 Guggenheim S, Bailey SW, Eggleton RA, Wilkes P. 1982. Structural aspects of greenalite and
454 related minerals. *Can. Mineral.* 20:1–18
- 455 Halevy I, Alesker M, Schuster EM, Popovitz-Biro R, Feldman Y. 2017. A key role for green rust
456 in the Precambrian oceans and the genesis of iron formations. *Nat. Geosci.* 10(2):135–39

457 Halevy I, Bachan A. 2017. The geologic history of seawater pH. *Science*. 355(6329):1069–71
458 Haugaard R, Pecoits E, Lalonde S, Rouxel O, Konhauser K. 2016. The Joffre banded iron
459 formation, Hamersley Group, Western Australia: Assessing the palaeoenvironment
460 through detailed petrology and chemostratigraphy. *Precambrian Res.* 273(Supplement
461 C):12–37
462 Hitchcock AP. 2014. aXis2000 is written in Interactive Data Language (IDL). It is available free
463 for non-commercial use from <<http://unicorn.mcmaster.ca/aXis2000.html/>>.
464 Humbert F, Sonnette L, de Kock MO, Robion P, Horng CS, et al. 2017. Palaeomagnetism of the
465 early Palaeoproterozoic, volcanic Hekpoort Formation (Transvaal Supergroup) of the
466 Kaapvaal craton, South Africa. *Geophys. J. Int.* 209(2):842–65
467 James HL. 1954. Sedimentary facies of iron-formation. *Econ. Geol. Bull. Soc. Econ. Geol.*
468 49(3):235–93
469 Johnson CM, Ludois JM, Beard BL, Beukes NJ, Heimann A. 2013. Iron formation carbonates:
470 Paleoceanographic proxy or recorder of microbial diagenesis? *Geology*. 41(11):1147–50
471 Johnson JE, Gerpheide A, Lamb MP, Fischer WW. 2014. O₂ constraints from Paleoproterozoic
472 detrital pyrite and uraninite. *Geol. Soc. Am. Bull.* 126(5–6):813–30
473 Kappler A, Newman DK. 2004. Formation of Fe(III)-minerals by Fe(II)-oxidizing
474 photoautotrophic bacteria 11Associate editor: L. G. Benning. *Geochim. Cosmochim.*
475 *Acta.* 68(6):1217–26
476 Klein C. 1974. Greenalite, stilpnomelane, minnesotaite, crocidolite and carbonates in a very low-
477 grade metamorphic Precambrian iron formation. *Can. Mineral.* 12(7):475–98
478 Klein C. 2005. Some Precambrian Banded Iron-Formations (BIFs) from Around the World:
479 Their Age, Geologic Setting, Mineralogy, Metamorphism, Geochemistry, and Origins.
480 *Am. Mineral.* 90(10):1473–99
481 Klein C, Beukes NJ. 1989. Geochemistry and sedimentology of a facies transition from
482 limestone to iron-formation deposition in the early Proterozoic Transvaal Supergroup,
483 South Africa. *Econ. Geol.* 84(7):1733–74
484 Komlos J, Kukkadapu RK, Zachara JM, Jaffé PR. 2007. Biostimulation of iron reduction and
485 subsequent oxidation of sediment containing Fe-silicates and Fe-oxides: Effect of redox
486 cycling on Fe(III) bioreduction. *Water Res.* 41(13):2996–3004
487 Konhauser KO, Amskold L, Lalonde SV, Posth NR, Kappler A, Anbar A. 2007. Decoupling
488 photochemical Fe(II) oxidation from shallow-water BIF deposition. *Earth Planet. Sci.*
489 *Lett.* 258(1):87–100
490 Konhauser KO, Ferris FG. 1996. Diversity of iron and silica precipitation by microbial mats in
491 hydrothermal waters, Iceland: Implications for Precambrian iron formations. *Geology*.
492 24(4):323–26
493 Konhauser KO, Pecoits E, Lalonde SV, Papineau D, Nisbet EG, et al. 2009. Oceanic nickel
494 depletion and a methanogen famine before the Great Oxidation Event. *Nature*.
495 458(7239):750–53
496 Konhauser KO, Urrutia MM. 1999. Bacterial clay authigenesis: a common biogeochemical
497 process. *Chem. Geol.* 161(4):399–413
498 Kostka JE, Haefele E, Viehweger R, Stucki JW. 1999. Respiration and Dissolution of Iron(III)-
499 Containing Clay Minerals by Bacteria. *Environ. Sci. Technol.* 33(18):3127–33
500 Krivovichev SV. 2013. Structural complexity of minerals: information storage and processing in
501 the mineral world. *Mineral. Mag.* 77(3):275–326

- 502 Laberge GL. 1986. A model for the biological precipitation of Precambrian iron-formation. .
503 <http://adsabs.harvard.edu/abs/1986ecgw.work...71L>
- 504 Leith CK. 1903. The Mesabi iron-bearing district of Minnesota. *U.S. Geol. Surv. Monograph*. 43
- 505 Li Z, Powell C, Bowman R. 1993. Timing and genesis of Hamersley iron-ore deposits. *Explor.*
506 *Geophys.* 24(3/4):631–36
- 507 Maliva RG, Knoll AH, Simonson BM. 2005. Secular change in the Precambrian silica cycle:
508 Insights from chert petrology. *GSA Bull.* 117(7–8):835–45
- 509 Miot J, Benzerara K, Morin G, Kappler A, Bernard S, et al. 2009. Iron biomineralization by
510 anaerobic neutrophilic iron-oxidizing bacteria. *Geochim. Cosmochim. Acta.* 73(3):696–
511 711
- 512 Miyano T, Beukes NJ. 1984. Phase relations of stilpnomelane, ferri-annite, and riebeckite in very
513 low-grade metamorphosed iron-formations. *South Afr. J. Geol.* 87(2):111–24
- 514 Pickard AL. 2002. SHRIMP U–Pb zircon ages of tuffaceous mudrocks in the Brockman Iron
515 Formation of the Hamersley Range, Western Australia*. *Aust. J. Earth Sci.* 49(3):491–
516 507
- 517 Posth NR, Canfield DE, Kappler A. 2014. Biogenic Fe(III) minerals: From formation to
518 diagenesis and preservation in the rock record. *Earth-Sci. Rev.* 135(Supplement C):103–
519 21
- 520 Posth NR, Köhler I, D. Swanner E, Schröder C, Wellmann E, et al. 2013. Simulating
521 Precambrian banded iron formation diagenesis. *Chem. Geol.* 362(Supplement C):66–73
- 522 Prasad N, Roscoe SM. 1996. Evidence of anoxic to oxic atmospheric change during 2.45–2.22
523 Ga from lower and upper sub-Huronian paleosols, Canada. *CATENA.* 27(2):105–21
- 524 Pufahl PK, Hiatt EE. 2012. Oxygenation of the Earth’s atmosphere–ocean system: A review of
525 physical and chemical sedimentologic responses. *Mar. Pet. Geol.* 32(1):1–20
- 526 Rasmussen B, Buick R. 1999. Redox State of the Archean Atmosphere: Evidence from Detrital
527 Heavy Minerals in Ca. 3250–2750 Ma Sandstones from the Pilbara Craton, Australia.
528 *Geology.* 27(2):115–18
- 529 Rasmussen B, Krapež B, Muhling JR, Suvorova A. 2015. Precipitation of iron silicate
530 nanoparticles in early Precambrian oceans marks Earth’s first iron age. *Geology.* 43:303–
531 6
- 532 Rasmussen B, Muhling JR, Suvorova A, Krapež B. 2016. Dust to dust: Evidence for the
533 formation of “primary” hematite dust in banded iron formations via oxidation of iron
534 silicate nanoparticles. *Precambrian Res.* 284(Supplement C):49–63
- 535 Rasmussen B, Muhling JR, Suvorova A, Krapež B. 2017. Greenalite precipitation linked to the
536 deposition of banded iron formations downslope from a late Archean carbonate platform.
537 *Precambrian Res.* 290(Supplement C):49–62
- 538 Rimstidt JD, Barnes HL. 1980. The kinetics of silica-water reactions. *Geochim. Cosmochim.*
539 *Acta.* 44(11):1683–99
- 540 Rye R, Holland HD. 1998. Paleosols and the evolution of atmospheric oxygen: a critical review.
541 *Am. J. Sci.* 298(8):621–72
- 542 Schaefer MV, Gorski CA, Scherer MM. 2011. Spectroscopic Evidence for Interfacial
543 Fe(II)–Fe(III) Electron Transfer in a Clay Mineral. *Environ. Sci. Technol.* 45(2):540–45
- 544 Siever R. 1992. The silica cycle in the Precambrian. *Geochim. Cosmochim. Acta.* 56(8):3265–72
- 545 Simonson BM. 2003. Origin and evolution of large Precambrian iron formations. In *Extreme*
546 *Depositional Environments: Mega End Members in Geologic Time*, eds. MA Chan, AW
547 Archer, pp. 231–44. Geological Society of America. Special Paper 370 ed.

- 548 Smith RE, Perdrix JL, Parks TC. 1982. Burial Metamorphism in the Hamersley Basin, Western
549 Australia. *J. Petrol.* 23(1):75–102
- 550 Spencer E, Percival FG. 1952. The structure and origin of the banded hematite jaspers of
551 Singhbhum, India. *Econ. Geol.* 47(4):365–83
- 552 Spurr JE. 1894. The iron-bearing rocks of the Mesabi Range in Minnesota. *10*
- 553 Stefurak EJT, Lowe DR, Zentner D, Fischer WW. 2014. Primary silica granules—A new mode
554 of Paleoarchean sedimentation. *Geology.* 42(4):283–86
- 555 Stefurak EJT, Lowe DR, Zentner D, Fischer WW. 2015. Sedimentology and geochemistry of
556 Archean silica granules. *GSA Bull.* 127(7–8):1090–1107
- 557 Sumner DY, Bowring SA. 1996. U-Pb geochronologic constraints on deposition of the
558 Campbellrand Subgroup, Transvaal Supergroup, South Africa. *Precambrian Res.* 79(1–
559 2):25–35
- 560 Sun S, Konhauser KO, Kappler A, Li Y-L. 2015. Primary hematite in Neoproterozoic to
561 Paleoproterozoic oceans. *GSA Bull.* 127(5–6):850–61
- 562 Tosca NJ, Guggenheim S, Pufahl PK. 2016. An authigenic origin for Precambrian greenalite:
563 Implications for iron formation and the chemistry of ancient seawater. *GSA Bull.* 128(3–
564 4):511–30
- 565 Urrutia MM, Beveridge TJ. 1994. Formation of fine-grained metal and silicate precipitates on a
566 bacterial surface (*Bacillus subtilis*). *Chem. Geol.* 116(3–4):261–80
- 567 Voegelin A, Senn A-C, Kaegi R, Hug SJ, Mangold S. 2013. Dynamic Fe-precipitate formation
568 induced by Fe(II) oxidation in aerated phosphate-containing water. *Geochim.*
569 *Cosmochim. Acta.* 117(Supplement C):216–31
- 570 Walker JCG. 1984. Suboxic diagenesis in banded iron formations. *Nature.* 309(5966):340–42
- 571 Webb SM. 2005. SIXpack: a graphical user interface for XAS analysis using IFEFFIT. *Phys.*
572 *Scr.* 2005(T115):1011
- 573 Winchell NH, Grant US, Todd JE, Upham W, Winchell HV. 1899. The Geology of Minnesota.
574 *Volume 4 of the Final Report.* 4
- 575 Wu W, Swanner ED, Hao L, Zeitvogel F, Obst M, et al. 2014. Characterization of the physiology
576 and cell-mineral interactions of the marine anoxygenic phototrophic Fe(II) oxidizer
577 *Rhodovulum iodosum*--implications for Precambrian Fe(II) oxidation. *FEMS Microbiol.*
578 *Ecol.* 88(3):503–15
- 579 Zegeye A, Bonneville S, Benning LG, Sturm A, Fowle DA, et al. 2012. Green rust formation
580 controls nutrient availability in a ferruginous water column. *Geology.* 40(7):599–602
- 581
- 582

583 **Main Text Figure Captions**

584

585 Fig 1: TEM Images and Diffractograms of Nanoparticle Inclusions

586 **A.** Five FIB foils of representative particles. Images on left indicate particle analyzed using
587 High-Resolution TEM imaging (right images) and Fast Fourier Transform (FFT, right panel) to
588 quantify the particle layering distance. Four samples had nanoparticles with d-spacings ~7.3-7.7
589 Ångstroms, while Silvergrass 313 m had some particles with 10 Ångstrom-spaced layers. Inset
590 with arrows for ABDP9 219 m indicate the ~20 Ångstrom superlattice reflections characteristic
591 of greenalite. **B.** Standards for Greenalite and Stilpnomelane show 7.6 Ångstrom spaced layers
592 for Greenalite and 10 Ångstrom spaced layers for Stilpnomelane.

593

594 Fig 2: Iron Redox Maps of Nanoparticle Inclusions in Chert

595 Sample FIB foils imaged using Scanning TEM (left) and Fe(III)/Fe_{Total} redox maps (right)
596 constructed using multiple energy STXM maps. Non-greenalite particles are outlined: pyrite
597 crystals (orange) and siderite crystals (yellow) were excluded from redox analyses, but a
598 different iron silicate (purple) was included in the iron silicate redox analysis. Scale bars 500 nm.

599

600 Fig 3: Mechanisms to Produce Low-Fe(III) Greenalite in Chert

601 Assuming seawater was at amorphous silica saturation, hypothetical pathways to form low-
602 Fe(III) greenalite encased in chert are:

603 (1) Greenalite exceeded saturation chemistry and precipitated.

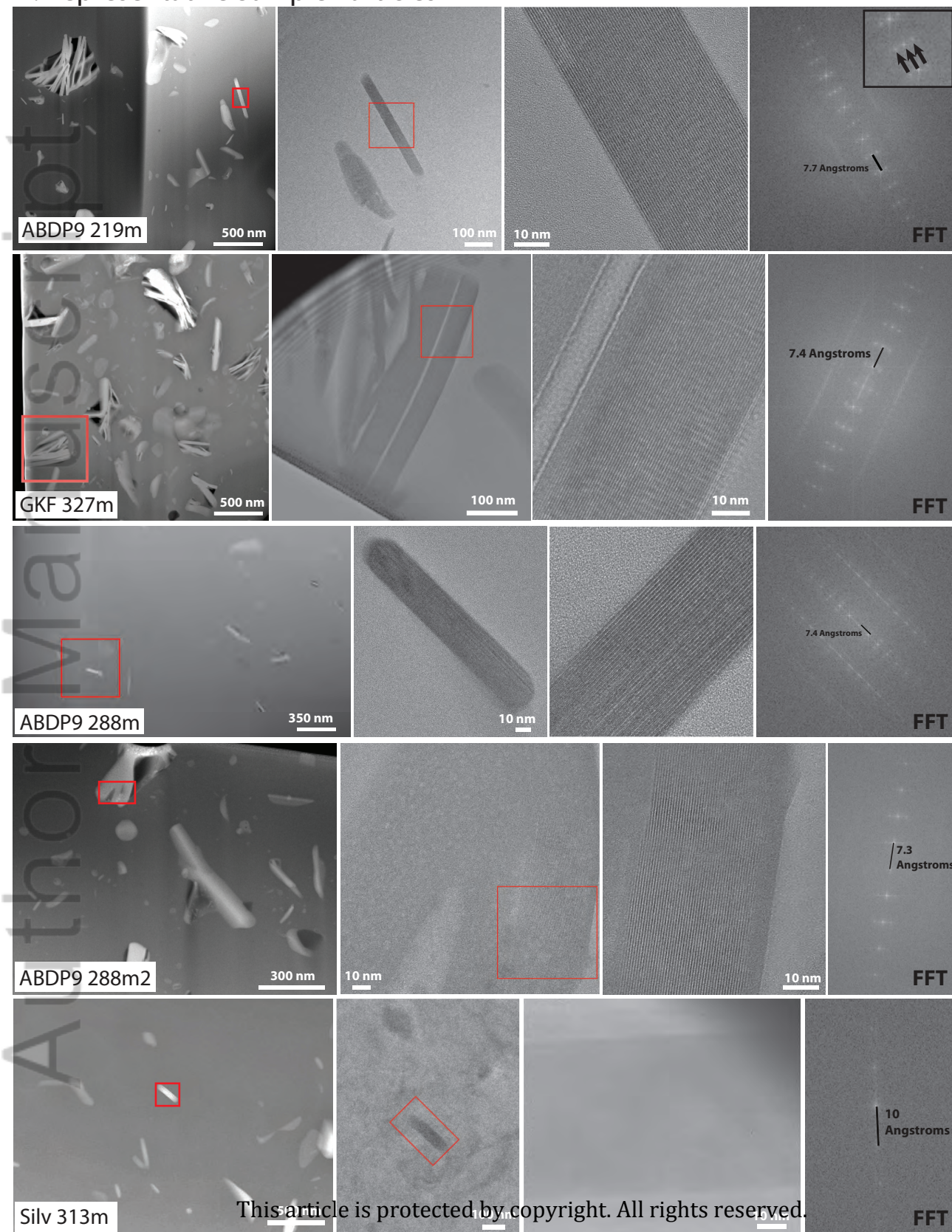
604 (2) Precipitation of Fe(II,III) greenalite catalyzed by the oxidation of aqueous Fe²⁺, either
605 abiotically or biologically mediated. A. Precipitation directly formed low-Fe(III) greenalite, or B.
606 Precipitation began as a high-Fe(III) greenalite, which then stabilized as low-Fe(III) greenalite.

607 (3) Oxidation of Fe²⁺ formed metastable green rust, which then transformed into low Fe(III)-
608 greenalite.

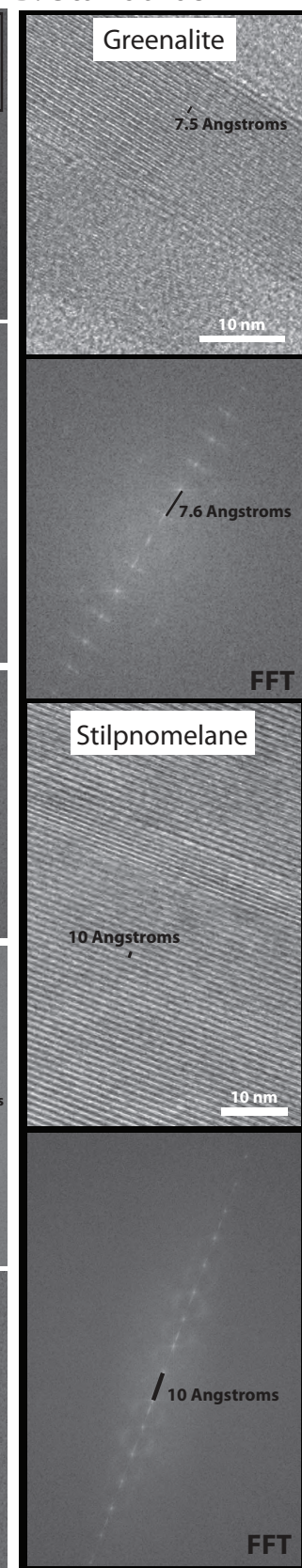
609 (4) Oxidation of Fe²⁺ formed precursor iron oxides and silica, which then transformed into low
610 Fe(III)-greenalite.

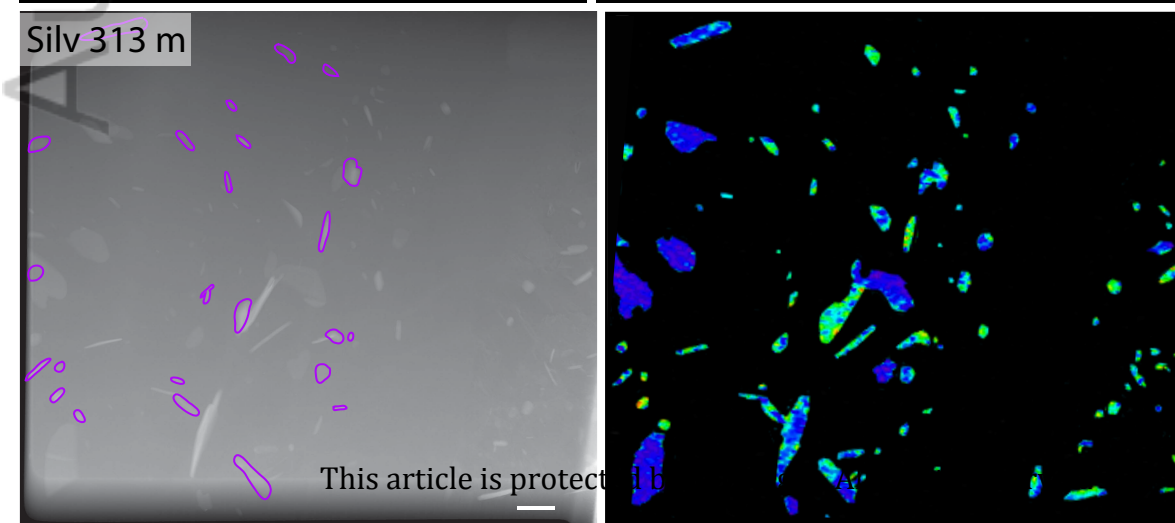
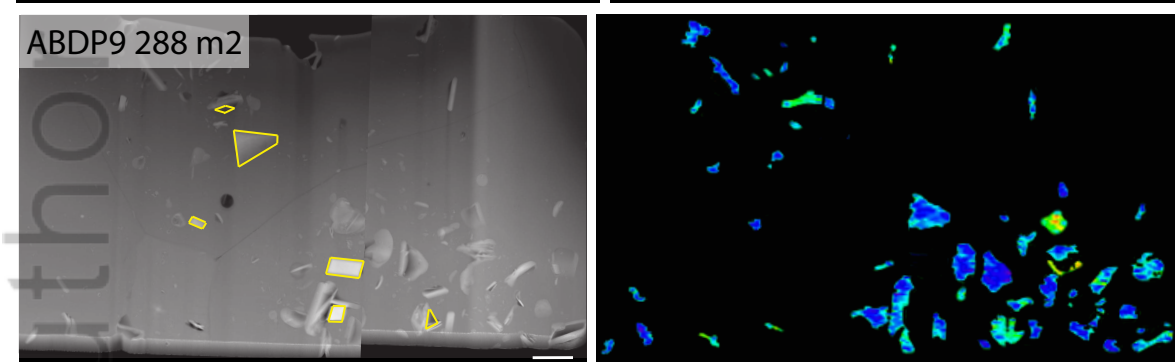
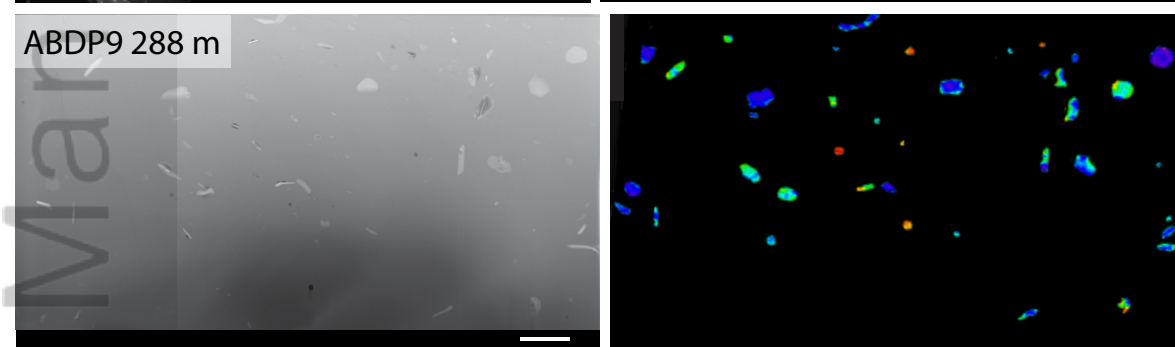
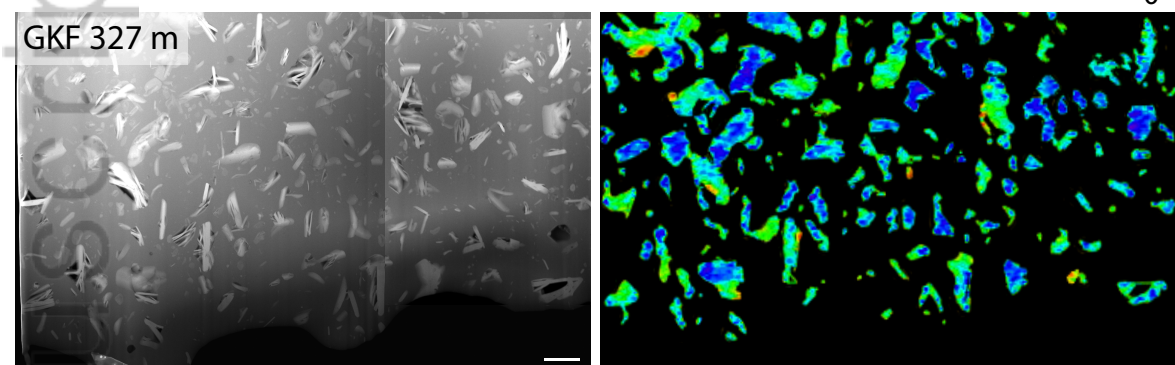
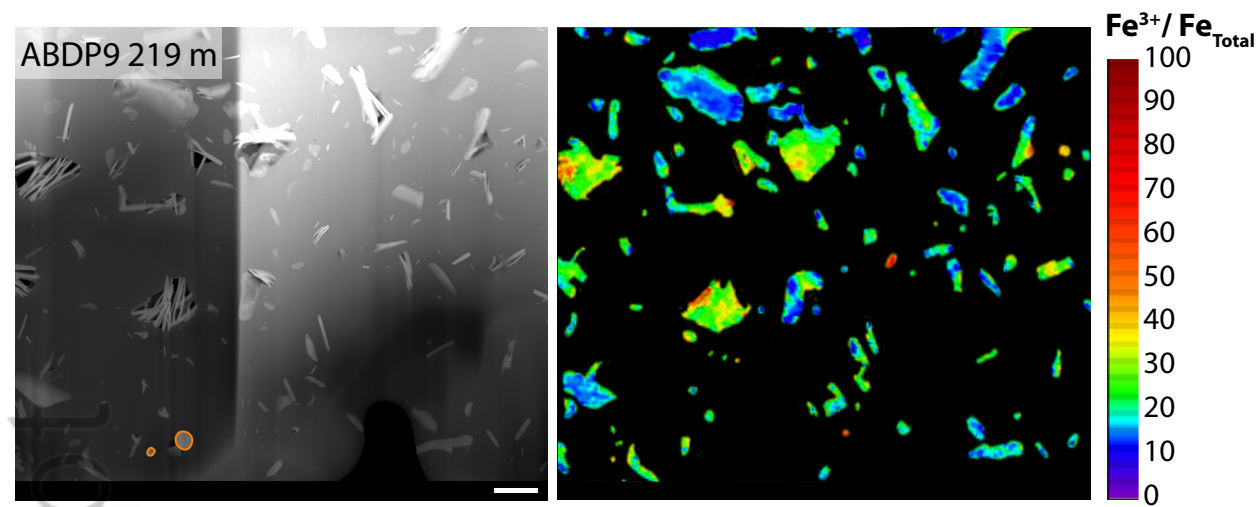
611

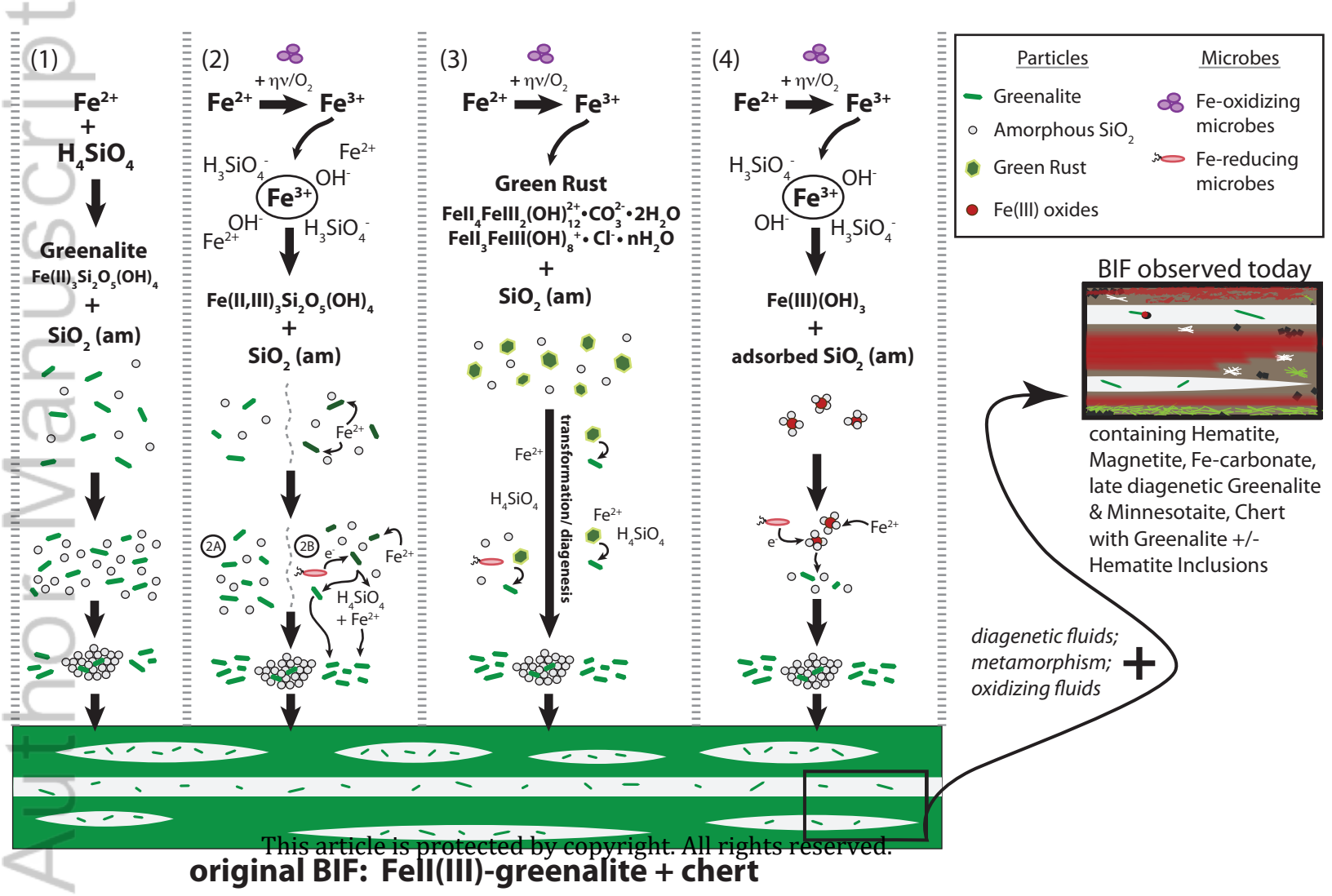
A. Representative Sample Particles



B. Standards







This article is protected by copyright. All rights reserved.
original BIF: Fe(III)-greenalite + chert